Journal of Materials Chemistry A

ROYAL SOCIETY OF CHEMISTRY

PAPER

View Article Online
View Journal | View Issue

Cite this: J. Mater. Chem. A, 2021, 9, 27380

Alleviated Mn^{2+} dissolution drives long-term cycling stability in ultrafine Mn_3O_4/PPy core–shell nanodots for zinc-ion batteries†

Le Jiang,[a] Fei Ye,[b] Zeyi Wu,[a] Lin Zhang,[a] Qiang Liu,[b] Zilong Tang [c] and Linfeng Hu *[ab]

Received 27th October 2021
Accepted 11th November 2021

DOI: 10.1039/d1ta09237e

rsc.li/materials-a

Aqueous Zn-ion batteries (ZIBs) have garnered significant attention regarding the growing demand for electrical energy, owing to their decent electrochemical performance, operational safety, low cost and environmental friendliness. However, optimization of cathode materials is still an issue and opportunity facing aqueous ZIBs. Organic coating is a common strategy to modify other types of cathode materials through the synergistic effect. Here, we synthesized a series of ultrafine Mn_3O_4/polypyrrole core–shell nanodot composites (Mn_3O_4/PPy) through an *in situ* polymerization strategy. The PPy content in this core–shell structure was continuously tuned by adjusting the pyrrole addition during self-polymerization. An optimized Mn_3O_4/PPy core–shell cathode with a PPy ratio of 14.6 wt% delivers a high capacity (332.5 mA h g^{-1} at 0.1 A g^{-1}) and excellent rate performance (141.7 mA h g^{-1} at 1 A g^{-1}). More importantly, Mn_3O_4/PPy shows superior long-term cycling stability over 1500 cycles (with a high capacity retention of 92.5% at 1.0 A g^{-1}), which is almost three times longer than that of pristine Mn_3O_4 nanodots. We have clarified that the improvement in long-term cycling stability is attributed to the increased electron/ion conductivity, alleviated Mn^{2+} dissolution and enhanced structural stability caused by PPy coating.

1. Introduction

Advanced energy storage technologies have stimulated considerable research interest regarding the growing demand for electrical energy.[1] Apart from traditional nonaqueous technologies, such as the lithium ion battery and sodium ion battery,[2,3] aqueous rechargeable battery technologies have garnered significant attention due to the low processing cost, environmental friendliness and operational safety.[4,5] Recently, aqueous Zn-ion batteries (ZIBs) emerged as promising alternatives owing to the advantages of decent electrochemical performance (theoretical gravimetric/volumetric capacities = 820 mA h g^{-1}/5855 mA h cm^{-3}), relatively low redox potential (−0.762 V *versus* standard hydrogen electrode), high natural abundance and exceptional inherent safety.[6–8]

Among the widely reported ZIB cathode materials, manganese-based materials are recognized as favourable host materials due to relatively high theoretical capacity, moderate operating voltage, a wide range of polymorphs and low cost.[9] Recently, we successfully developed a series of manganese-based spinel oxide nanodots (Mn_3O_4, $CoMn_2O_4$, $MnCo_2O_{4.5}$, Co_3O_4, and $ZnMn_2O_4$) as the cathode materials for aqueous ZIBs. Among them, Mn_3O_4 nanodots deliver the highest reversible capacity of 386.7 mA h g^{-1} at 0.1 A g^{-1}.[23] Unfortunately, the optimal Mn_3O_4 nanodots just cycled 500 times at a relatively low current density of 0.5 A g^{-1} suffering from low intrinsic electronic conductivity and inevitable Mn^{2+} dissolution.[10] Such a limited cycling lifespan cannot meet the growing demand for portable electronics, transportation, grid-storage application, *etc.*

The organic/manganese oxide composite strategy, coating or intercalation of a conductive polymer as an example, could modify other types of cathode materials through the synergistic effect.[11] Typically, Xia *et al.* figured out that polyaniline (PANI) strengthened the layered structure of manganese dioxide and the composite obtains a long-term stability of 200 cycles at a utilization of 90%.[12] Hu *et al.* successfully created a poly(3,4-ethylenedioxythiophene) (PEDOT) coating shell contributing to fast zinc^{2+}/electron transport kinetics and protection from structural collapse during cycling.[13]

Motivated by this progress of organic/inorganic composites in ZIBs, herein, we successfully developed ultrafine Mn_3O_4/polypyrrole (Mn_3O_4/PPy) core–shell nanodots through an *in situ*

[a]Department of Materials Science, Fudan University, Shanghai 200433, P. R. China. E-mail: linfenghu@seu.edu.cn

[b]School of Materials Science and Engineering, Southeast University, Nanjing, 211189, P. R. China

[c]State Key Laboratory of New Ceramics and Fine Processing, School of Materials Science and Engineering, Tsinghua University, Beijing 100084, China

† Electronic supplementary information (ESI) available. See DOI: 10.1039/d1ta09237e

self-polymerization process. The PPy content in this core–shell structure was easily tuned by adjusting the pyrrole addition during polymerization. The optimized Mn_3O_4/PPy core–shell cathode with a PPy ratio of 14.6 wt% delivers a high capacity (332.5 mA h g^{-1} at 0.1 A g^{-1}), excellent rate performance (141.7 mA h g^{-1} at 1 A g^{-1}), and superior long-term cycling stability over 1500 cycles with a high capacity retention of 92.5% at 1.0 A g^{-1}. This robust lifespan is almost three times longer than that of pristine Mn_3O_4 nanodots. The improvement in long-term cycling stability is attributed to the increased electron/ion conductivity, alleviated Mn^{2+} dissolution and enhanced structural stability caused by PPy coating.

2. Results and discussion

Mn_3O_4/PPy core–shell nanodots were prepared through an *in situ* self-polymerization of pyrrole monomers on the surface of Mn_3O_4 nanodots, as illustrated in Fig. 1a. HCl was added to form active sites on the surface of Mn_3O_4 nanodots. With the addition of 400 μL pyrrole and subsequent stirring, the color of the suspension changed from brown to dark brown. Transmission electron microscopy (TEM) observation reveals a large number of nanodot-like objects with an average size of 8.0 nm (Fig. 1b and S1†). A representative high-resolution TEM image (HRTEM, Fig. 1c) shows clear lattice fringe spacings of 2.5, 2.8 and 3.1 Å, which, respectively, correspond to the (202), (103) and (112) planes of tetragonal Mn_3O_4 with the space group $I4_1/amd$ (JCPDS no. 80-0382). One can clearly distinguish the PPy coating layer with a thickness of ~1 nm (marked by dotted lines) outside the Mn_3O_4 nanodots, demonstrating the successful formation of a "PPy shell/Mn_3O_4 core" structure. The selected area electron diffraction (SAED, Fig. 1d) pattern obtained from several nanodots exhibits typical diffraction rings with a polycrystalline nature. The X-ray diffraction (XRD) pattern of Mn_3O_4/PPy composites in Fig. 1e is similar to that of pristine Mn_3O_4, indicating that the crystallinity is well maintained after PPy coating. The peaks at 2θ of 28.9°, 32.4°, 36.1°, 58.5° and 59.9° can be indexed to the (112), (103), (211), (321) and (224) planes of the tetragonal Mn_3O_4. Note that a broad diffraction peak from 20° to 30° attributed to the amorphous PPy emerges in the Mn_3O_4/PPy composites.[14–16]

The presence of the PPy layer in the Mn_3O_4 host was further confirmed from Fourier Transform Infrared Spectroscopy (FTIR, Fig. 1f) and Raman scattering spectra (Fig. 1g). For both pristine Mn_3O_4 and Mn_3O_4/PPy composites, two high-intensity FTIR absorption bands at 620 and 500 cm^{-1} could be assigned to the stretching vibration of Mn–O bonds at octahedral (Mn^{3+}) and tetrahedral (Mn^{2+}) sites.[17] The high-resolution FTIR spectrum (4000–700 cm^{-1}) of Mn_3O_4/PPy nanodots is shown in Fig. S2,† in which typical peaks of the PPy layer are evident. The peaks situated at 1630 and 1557 cm^{-1} are associated with the stretching of the C=C or C–C bonds and the fundamental vibrations of the pyrrole-ring.[18,19] The bands located at 1427 and 1345 cm^{-1} could be attributed to the C–N stretching vibration,[16] and those at 1256 and 887 cm^{-1} are attributed to the =C–H in-plane and out-plane bending vibrations.[15] The broad bands from 3500 to 2500 cm^{-1} represent the C–H or N–H stretching mode.[16] The Raman spectrum of the Mn_3O_4/PPy composites is composed of absorption peaks of both pure PPy and Mn_3O_4 nanodots. As shown in Fig. 1g, the strong phonon band centered at 648 cm^{-1} is ascribed to the A_{1g} spectroscopic species with Mn–O symmetric vibration, and those with lower scattering intensity in the range from 200 to 480 cm^{-1} are assigned to Mn–O bending vibration.[20] The peaks at 1317 cm^{-1} and 1575 cm^{-1} correspond to the phonon modes of PPy with anti-symmetrical C–N stretching and C=C stretching, which proves the existence of PPy in the sample.[21]

X-ray photoelectron spectroscopy (XPS) was performed to analyze the detailed chemical environment of atoms in pure Mn_3O_4 and Mn_3O_4/PPy composites. As presented in Fig. 1h, the XPS spectrum of our Mn_3O_4/PPy nanodots provides evidence for four characteristic peaks of Mn, O, N and C. High-resolution XPS spectra of Mn 2p, O 1s, C 1s, and N 1s for Mn_3O_4/PPy nanodots are depicted in Fig. S3.† The two sets of Mn 2p spin–orbit doublets in Fig. S3a† can be resolved into Mn^{3+} 2p parts (642.2 and 653.8 eV) and Mn^{2+} 2p parts (641.1 and 652.8 eV).[22] The O 1s spectrum in Fig. S3b† represents typical Mn–O–Mn (529.9 eV), Mn–O–H (531.5 eV) and H–O–H (532.7 eV) bonds.[23] The C 1s spectrum in Fig. S3c† can be resolved into two components centered at 284.7 eV and 285.7 eV, which are related to C–C/C=C and C–N/C=N bonding.[15] The N 1s spectrum in Fig. S3d† fits with three peaks at 397.3 eV, 399.7 eV and 401.3 eV, corresponding to C–N=, C–NH– and C–N^+– bonds, respectively.[24]

Subsequently, we assembled conventional CR2032 coin cells to assess the electrochemical performance with regard to Zn-ion storage of our Mn_3O_4/PPy nanodot cathode. According to the reversible cyclic voltammetry (CV) test from 0.1 to 0.5 mV s^{-1} (Fig. 2a), an overlapped oxidation peak is observed at around 1.56 and 1.61 V, and two distinct reduction peaks are observed at 1.23 and 1.36 V, which could be, respectively, ascribed to the insertion/extraction of Zn^{2+} and H^+ from the material in accordance with previous studies.[22,23] The peaks of the CV curves gradually grow broad with the increase of scan rate, while the shapes remain basically consistent. It is known that CV data at various scan rates could be analyzed in terms of the equation $i_{peak} = a\nu^b$, where i_{peak} is the peak current, ν is the scan rate, and a, b are adjustable values. A b value of 0.5 is representative of a diffusion-controlled insertion process, while a b value of 1.0 is indicative of a surface-controlled capacitive process.[25,26] Therefore, the current I at a fixed potential could be divided into two parts, the diffusion-controlled part $C_1\nu^{1/2}$ and the capacitive-controlled part $C_2\nu$ (C_1 and C_2 are adjustable values).[27,28] The dependence of $\log(i_{peak})$ and $\log(\nu)$ at various scan rates is given in Fig. 2b. The b values could be determined using the slope of the $\log(i_{peak}) - \log(\nu)$ plots, which are 0.90, 0.81, 0.80, and 0.89 for the four redox peaks O_1, O_2, R_1, and R_2, respectively. The contribution rate of the capacitive effect (Fig. 2c and S4†) is calculated to be 68.0%, 71.4%, 74.0%, 75.4%, and 76.3% at the scan rates of 0.1, 0.2, 0.3, 0.4, and 0.5 mV s^{-1}, respectively. This suggests that the electrochemical kinetics of the Mn_3O_4/PPy nanodot electrode is bound up with both diffusion-controlled and capacitive-controlled effects. The diffusion-controlled behavior plays a major role in the whole capacity contribution to Zn-ion storage. A gradual increase of the capacitive effect could be observed with the increase of the scan rate, which was

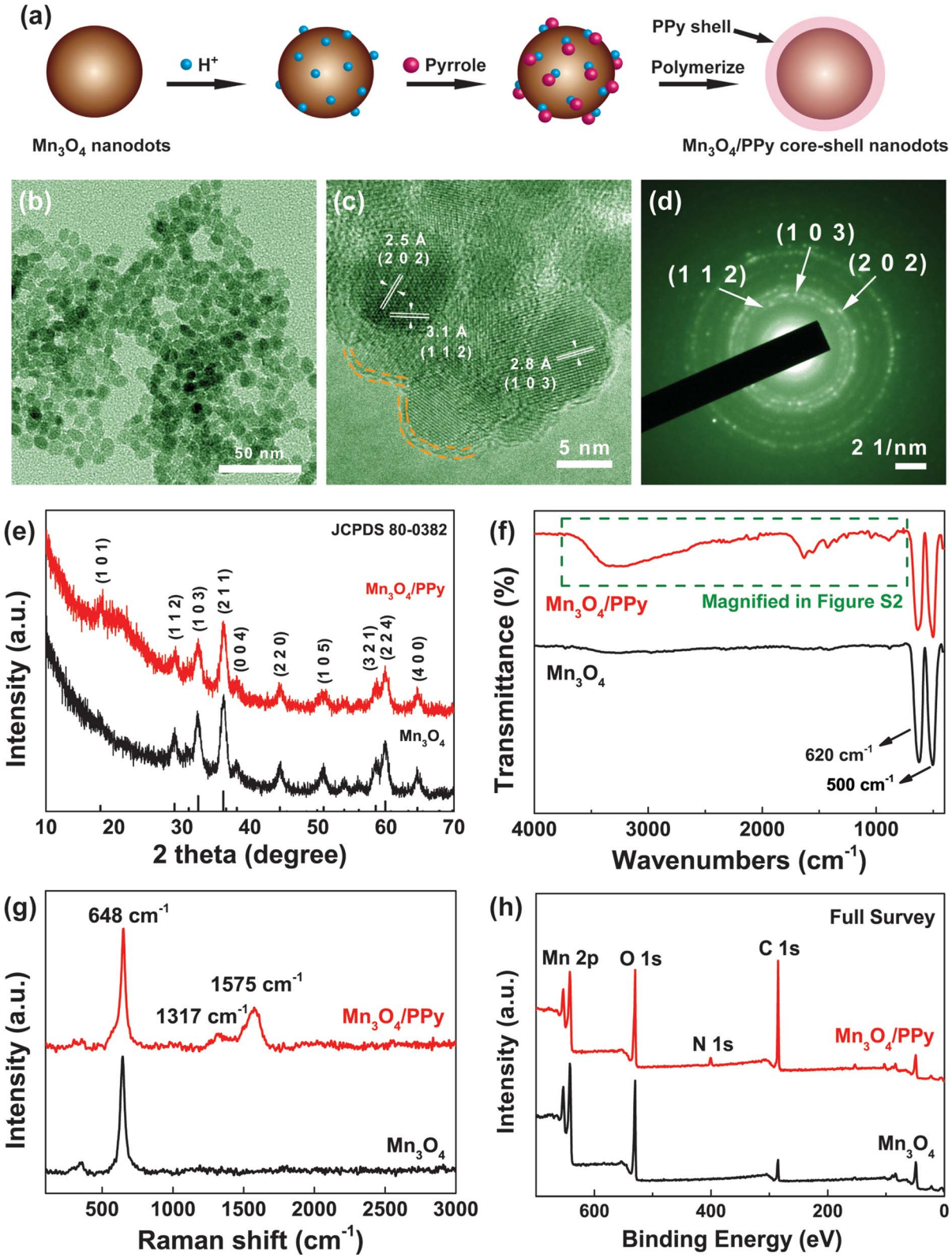

Fig. 1 (a) Schematic illustration of the synthetic process of the Mn_3O_4/PPy core–shell nanodots. (b) Typical TEM image of Mn_3O_4/PPy core–shell nanodots. (c) HRTEM images and (d) the corresponding SAED pattern. (e) XRD patterns, (f) Raman scattering, (g) FTIR spectra, and (h) XPS spectra of Mn_3O_4 and Mn_3O_4/PPy nanodots, respectively.

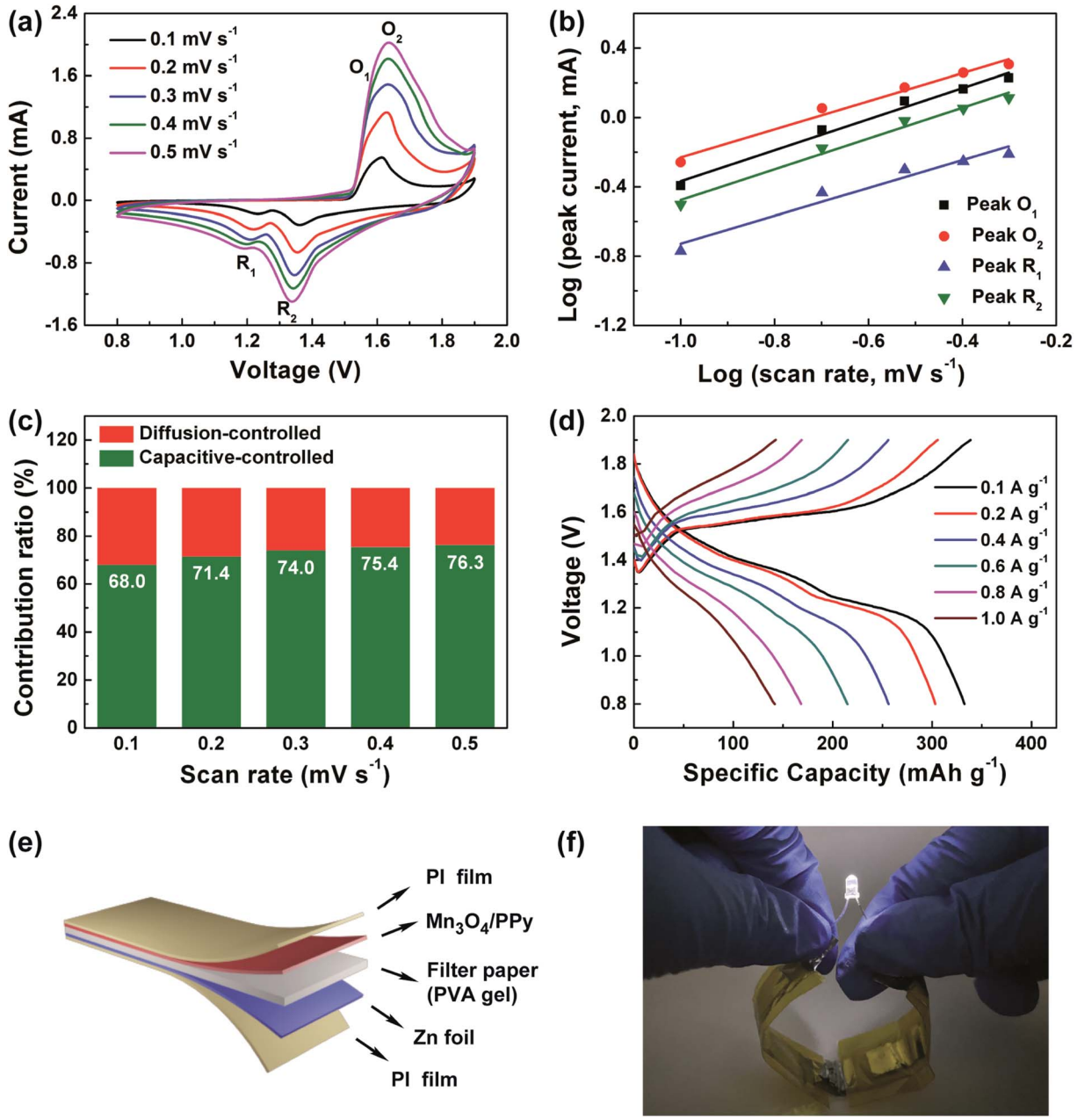

Fig. 2 (a) CV curves of the Mn_3O_4/PPy nanodot electrode at various scan rates from 0.1 to 0.5 mV s^{-1}. (b) The corresponding log i_{peak} *vs.* log ν plots at four different oxidation/reduction states. (c) Contribution ratio of capacitive and diffusion-controlled capacities at different scan rates. (d) Charge/discharge profiles of the as-assembled Zn–Mn_3O_4/PPy coin cell tested at different current densities. (e) Schematic structure of the flexible Zn–Mn_3O_4/PPy battery. (f) Photograph of a white light-emitting diode indicator lighted by two sets of batteries in series.

also detected in the Mn_3O_4 nanodot electrode in our previous report.[23] Fig. 2d shows the galvanostatic charge/discharge (GCD) curves of the Zn–Mn_3O_4/PPy coin cell tested at different current densities. The two plateaus of H^+ and Zn^{2+} insertion/extraction gradually become indiscernible with the increase of current density. The as-assembled cell delivers reversible capacities of 332.5, 303.1, 256.3, 204.8, 168.7 and 141.7 mA h g^{-1}, respectively, at current densities of 0.1, 0.2, 0.4, 0.6, 0.8 and 1.0 A g^{-1}.

Electrochemical impedance spectra (EIS) measurements clarified the electrochemical kinetics in the Mn_3O_4/PPy core–shells. From the Nyquist plots before cycling (Fig. S5†), the plots of Mn_3O_4/PPy composites show lower series resistance (R_s) than those of pristine Mn_3O_4 nanodots, demonstrating that the introduction of PPy remarkably increases the ion conductivity of Mn_3O_4 nanodots. Due to the increased conductivity, the Mn_3O_4/PPy cathode displays an improved rate capability and a considerable recovered capacity when the current density was decreased back to 0.1 A g^{-1} (Fig. S6†). Note that a smaller semicircle emerges between the region of series resistance and charge transfer resistance in Mn_3O_4/PPy. The semicircle reflects the interface resistance between the liquid electrolyte and solid

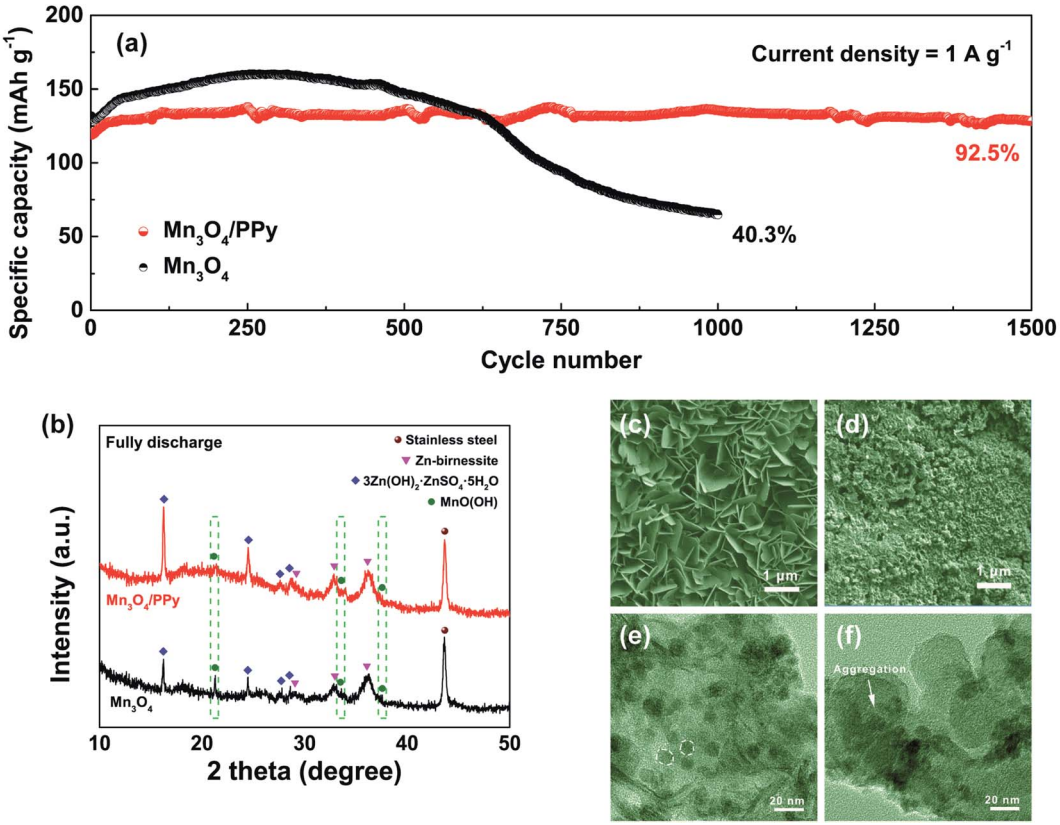

Fig. 3 (a) Cycling performance of the as-assembled Zn//Mn_3O_4 and Zn//Mn_3O_4/PPy coin cells at 1.0 A g^{-1}. (b) *Ex situ* XRD of the Mn_3O_4 and Mn_3O_4/PPy cathode when fully discharged. SEM images of the fully (c) discharged and (d) charged Mn_3O_4/PPy cathode. TEM images of the resulting (e) Mn_3O_4/PPy and (f) Mn_3O_4 cathode after 1000 cycles. The two-dimensional plate-like objects should be PVDF in the cathode.

electrode interface, and should be ascribed to the enhanced hydrophobicity of the PPy shell.[29] Galvanostatic intermittent titration technique (GITT) measurements were conducted to further investigate the ion diffusion kinetics in our Mn_3O_4/PPy core–shell sample. A galvanostatic charge/discharge operation for 10 min and a relaxation process for a 10 min take turns in the test (Fig. S7†). The Brunauer–Emmett–Teller (BET) method was performed to obtain the specific surface area of our sample for further calculation (Fig. S8†). The Mn_3O_4/PPy nanodot cathode exhibits high diffusion coefficients, 4.5×10^{-10} cm^2 s^{-1} for D_H (Region II) and 4.0×10^{-11} cm^2 s^{-1} for D_{Zn} (Region I).[30]

With the increasing interest in wearable and miniaturized electronics, energy storage devices with excellent flexibility have attracted significant attention.[31–33] Thus, we fabricated a quasi-solid-state Zn-ion battery based on the Mn_3O_4/PPy cathode to broaden its flexible application in the wearable electronics field. As illustrated in Fig. 2e, each layer was assembled with a simple lamination process in ambient air. Zinc foil and stainless steel (SS) foil coated with Mn_3O_4/PPy was separated by using a filter paper infused with PVA gel electrolyte, and the pressed layers were sealed with polyimide (PI) film to form a stable sandwich structure. One can see that a white light-emitting diode (LED) indicator (~3 V) (Fig. 2f) could be lighted by two sets of batteries in series. The charge/discharge curves of a single flexible battery remain nearly unchanged within 10 cycles at different bending angles (Fig. S9†), indicating the promising potential to develop high-performance flexible and portable devices.

Particularly, long-term cycling stability with a high capacity retention ratio is very essential for practical applications. As shown in Fig. 3a, the pristine Mn_3O_4 nanodots just show cycling stability within 500 cycles, and apparent capacity decay occurs after this lifespan with a low capacity retention ratio of 40.3% after 1000 cycles at 1.0 A g^{-1}. In contrast, our Mn_3O_4/PPy core–shell cathode delivers much superior cycling performance over 1500 cycles. The reversible capacity of the Mn_3O_4/PPy cathode is 137.9 mA h g^{-1} with a much higher capacity retention of 92.5%. Moreover, the Mn_3O_4/PPy cathode shows superiority in cycling stability irrespective of whether electrolyte $MnSO_4$ salt is added or not in the electrolyte solution (Fig. S10†). Fig. S11 in the ESI† shows the charge/discharge profiles of Mn_3O_4 and Mn_3O_4/PPy cathodes at various cycles during the long-term lifespan. One can see that these two discharge plateaus corresponding to proton and zinc-ion intercalation gradually merge into one at 1.0 A g^{-1} in both cathodes. Furthermore, the pristine Mn_3O_4 cathode presents significant decay in plateau and capacity after 500 cycles. In contrast, the discharge plateau and capacity of the Mn_3O_4/PPy cathode were well retained even after a long cycling for 1500 cycles.

As confirmed in Fig. S5,† PPy coating improves the electron and ion conductivity of Mn_3O_4, which is favorable for excellent cycling stability during long-term charge/discharge. To get

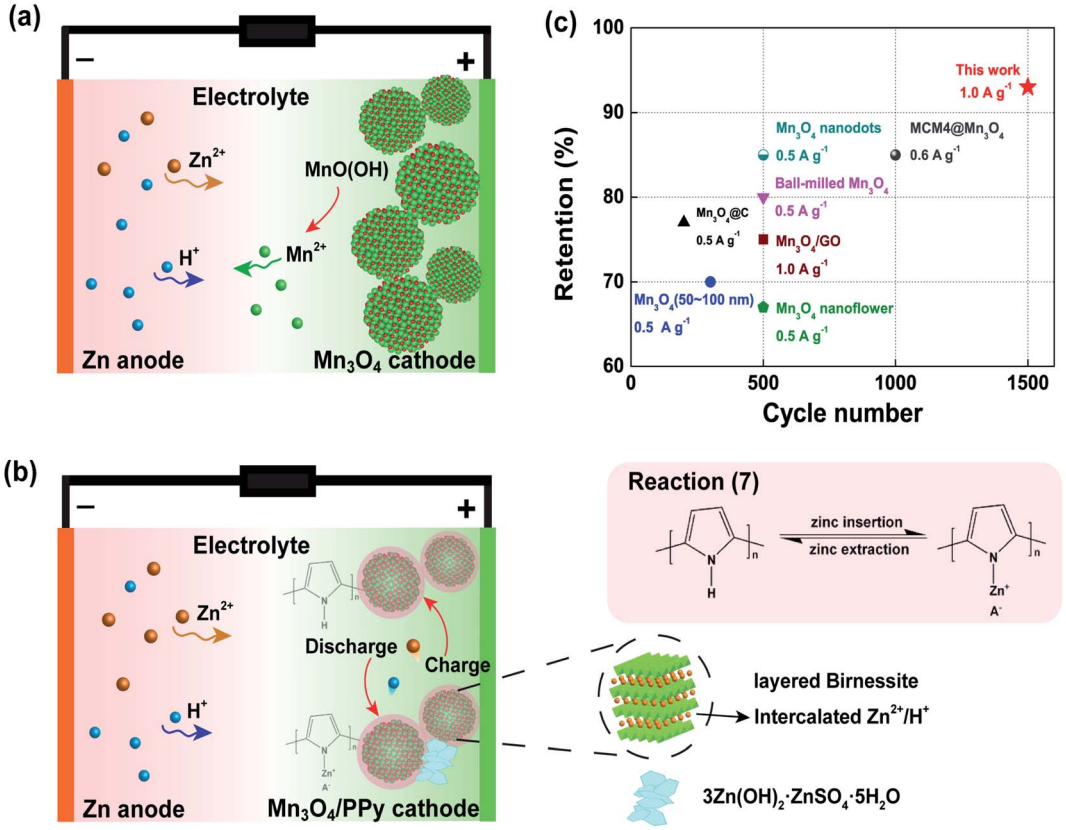

Fig. 4 Schematic representation of the reaction mechanism in (a) Zn–Mn_3O_4 and (b) Zn–Mn_3O_4/PPy batteries. The reaction pathway of PPy during Zn insertion/extraction shown in reaction (7).[44] (c) The comparison of cycling performances of various Mn_3O_4-related cathode materials in ZIBs.[23,30,35,48–52]

a deeper understanding of long-term stability, *ex situ* XRD characterization was further carried out to clarify the detailed phase evolution during the electrochemical process (Fig. 3b). Compared with the original cathodes before charge/discharge cycles (Fig. S12†), the diffraction peaks from Zn–birnessite, $3Zn(OH)_2 \cdot ZnSO_4 \cdot 5H_2O$ (JCPDS no. 39-0688) and MnO(OH) (JCPDS no. 88-0648) can be detected when fully discharged in the first cycle, respectively, identifying that H^+ and Zn^{2+} reactions both participate in Mn_3O_4 and Mn_3O_4/PPy cathodes.[34,35] It is worth noting that the Mn_3O_4/PPy and pure Mn_3O_4 cathodes deliver different diffraction intensities for the MnO(OH) intermediate product in Fig. 3b, in which the former shows much weaker diffraction peaks than the latter. According to Liang's recent study on the Zn//MnO_2 battery chemistry, a dissolution–deposition mechanism has been proposed and subsequently confirmed, in which Mn_3O_4 converts to the birnessite phase ($MnO_2 \cdot nH_2O$) with the insertion of H_2O and Mn^{2+} dissolution into the electrolyte in the first charge process.[36]

$$2Mn_3O_4 + nH_2O \rightarrow 4\ \text{birnessite–}MnO_2 \cdot nH_2O + 2Mn^{2+} + 4e^- \quad (1)$$

After this irreversible transformation, the H^+ and Zn^{2+} intercalation/de-intercalation mechanism (reaction (2) and (3)) and also a conversion reaction process (reaction (4)) would be coexistent in the Zn//MnO_2 battery system.[31,36] In general, the formation of the MnO(OH) intermediate in reaction (4) has great impacts on long-term cyclability in manganese-based aqueous ZIBs.[1,8] This MnO(OH) intermediate is unstable in aqueous electrolyte solutions due to the Jahn–Teller effect.[37] Subsequently, the disproportionation reaction between MnO(OH) and protons results in the dissolution of birnessite–$MnO_2 \cdot nH_2O$ in the cathode and drastic capacity fading (reaction (5), Fig. 4a).[38] In our case, the above-mentioned lower diffraction intensity of the MnO(OH) intermediate detected in the Mn_3O_4/PPy cathode indicates that reaction (5) was significantly inhibited during the discharge process. In contrast, the favorable formation of MnO(OH) in the pristine Mn_3O_4 sample gives rise to more opportunities for disproportionation and Mn^{2+} dissolution during the electrochemical process.[39] Such a difference in Mn^{2+} dissolution behaviour should be an important reason for the cycling stability enhancement in the Mn_3O_4/PPy cathode.

$$\text{Birnessite–}MnO_2 \cdot nH_2O + xH^+ + xe^- \rightleftharpoons H_xMnO_2 + nH_2O \quad (2)$$

$$H_xMnO_2 + yZn^{2+} + 2ye^- \rightleftharpoons H_xZn_yMnO_2\ (\text{Zn–birnessite}) \quad (3)$$

$$\text{Birnessite–}MnO_2 \cdot nH_2O + H^+ + e^- \rightleftharpoons MnO(OH) + nH_2O \quad (4)$$

$$2MnO(OH) + 2H^+ \rightarrow MnO_2 + Mn^{2+} + 2H_2O\ (Mn^{2+}\ \text{dissolution}) \quad (5)$$

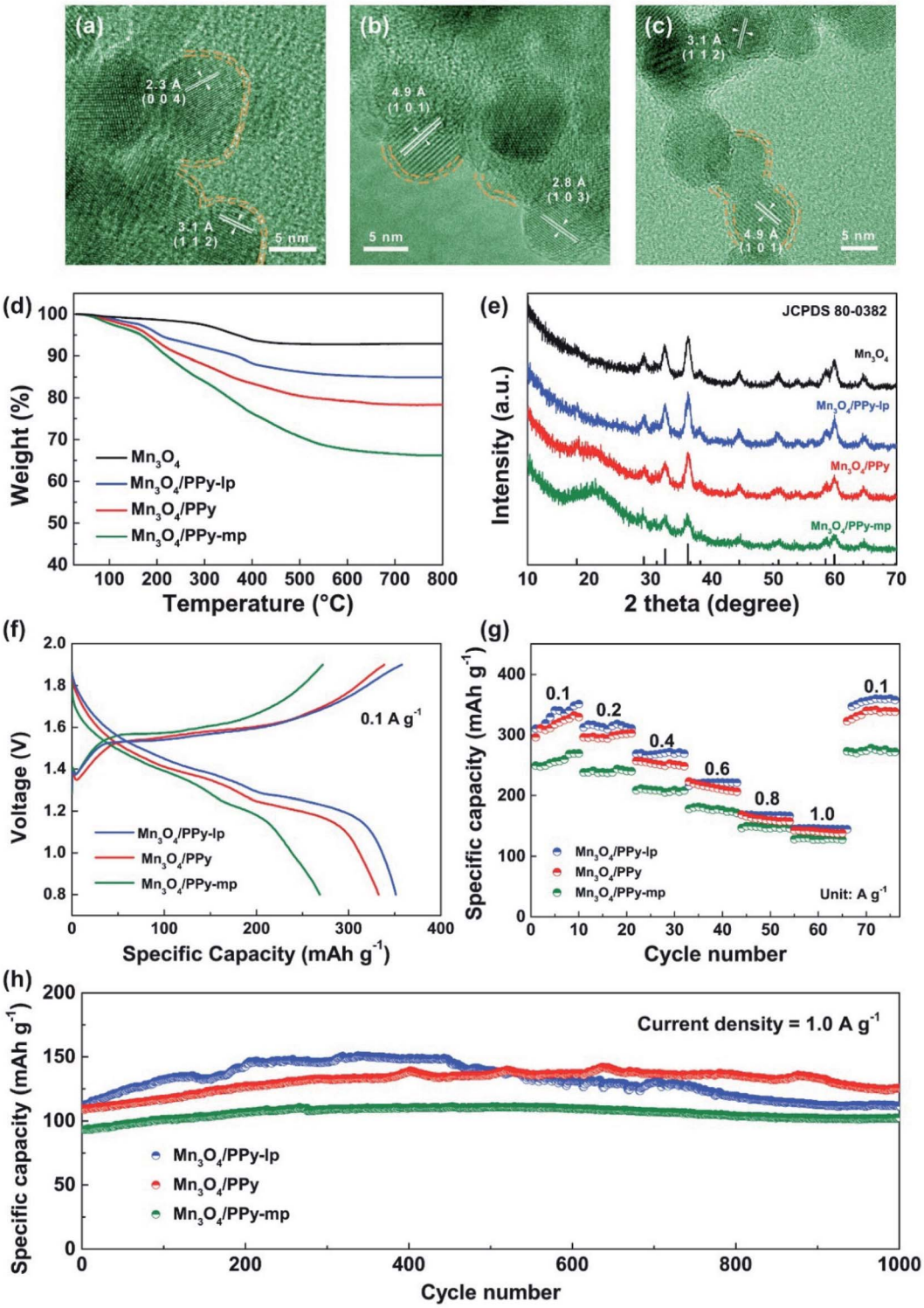

Fig. 5 HRTEM image of (a) Mn_3O_4/PPy-lp, (b) Mn_3O_4/PPy, and (c) Mn_3O_4/PPy-mp nanodots. (d) TGA curves and (e) XRD patterns of the as-prepared nanodots. (f) Galvanostatic charge/discharge curves at 0.1 A g^{-1}, (g) rate and (h) cycling performance of the as-prepared composites with different pyrrole addition.

On the other hand, the concentration of OH^- ions greatly increases and basic zinc hydroxide sulfate is gradually formed on the surface of the cathode:

$$4Zn^{2+} + 6OH^- + SO_4^{2-} + 5H_2O \rightleftharpoons 3Zn(OH)_2 \cdot ZnSO_4 \cdot 5H_2O \quad (6)$$

Previous studies have identified that $3Zn(OH)_2 \cdot ZnSO_4 \cdot 5H_2O$ is generally crystallized into a two-dimensional nanoflake-like

morphology.[40,41] In our case, we also observed such nanoflake arrays on the Mn_3O_4/PPy electrode surface after long-term cycling by scanning electron microscopy (SEM) (Fig. 3c). Upon charging, the released H^+ would decrease the pH value again and dissolve the $3Zn(OH)_2 \cdot ZnSO_4 \cdot 5H_2O$ precipitate back into the electrolyte.[42] One can see in Fig. 3d that $3Zn(OH)_2 \cdot ZnSO_4 \cdot 5H_2O$ nanoflake arrays mostly disappear when fully charged, demonstrating the excellent reversibility of reaction (6). Note that the reversible precipitation/dissolution process of $3Zn(OH)_2 \cdot ZnSO_4 \cdot 5H_2O$ also plays an important role in cycling stability, which buffers the electrolyte pH change and sustains the proton insertion mechanism.[43] Such a schematic reaction mechanism in our Zn//Mn_3O_4/PPy battery is illustrated in Fig. 4b.

Additionally, the geometrical configuration of both cathodes was investigated by TEM observation as shown in Fig. 3e and f. It is clear that Mn_3O_4/PPy nanodots can well retain their initial monodisperse core–shell morphology after long charge/discharge cycles (Fig. 3e). However, pure Mn_3O_4 nanodots without a PPy coating generally lost their nanodot morphology with drastic aggregation (Fig. 3f). Previous reports reveal that the polymer coating is able to confine active materials in a physical way and accommodate the strains related to volume changes.[45,46] It is rational that the PPy shell successfully constructs a protective layer and should also act on restraining the stress of volume expansion and maintaining structural stability.[45,47] The enhanced structural stability should be another origin of the superior cycling lifespan for our Mn_3O_4/PPy core–shells.

Having realized the remarkable enhancement in long-term lifespan in a Zn//MnO_2 aqueous battery system, we now compare our specific capacity and cycling stability with those of various Mn_3O_4-related cathode materials recently reported (Fig. 4c and Table S1†). It is clear that the specific capacity, long-term lifespan and capacity retention of our Mn_3O_4/PPy core–shell nanodots surpass those of most of the conventional Mn_3O_4-related materials including Mn_3O_4 nanodots,[23] Mn_3O_4 nanoflowers,[30] Mn_3O_4 (50–100 nm),[35] Mn_3O_4@C,[48] ball-milled Mn_3O_4,[49] MCM4@Mn_3O_4,[50] Mn_3O_4@NC,[51] and Mn_3O_4/GO.[52]

Finally, the influence of the regulation of PPy content in the core–shell structures on the electrochemical properties was further studied. We found that the PPy content in Mn_3O_4/PPy composites can be continuously tuned by changing the pyrrole addition during the *in situ* self-polymerization process (Fig. 5a–c and S13†). The samples with pyrrole addition of 200 μL, 400 μL and 800 μL were labelled Mn_3O_4/PPy-lp, Mn_3O_4/PPy, and Mn_3O_4/PPy-mp, respectively. Thermogravimetric analysis (TGA) curves (Fig. 5d) exhibit three weight losses of 8.0%, 14.6% and 26.7% of Mn_3O_4/PPy-lp, Mn_3O_4/PPy, and Mn_3O_4/PPy-mp samples, respectively. The initial weight loss below 200 °C is due to the adsorbed water.[24] The significant weight loss of the composites starts at about 200 °C, which corresponds to the degradation of PPy.[14] In addition, the broad PPy diffraction peaks located at $2\theta = 20°–25°$ become more apparent with the increasing ratio of pyrrole addition (Fig. 5e).[15,18] Aqueous ZIB performances based on these cathodes are compared in Fig. 5f–h. The three galvanostatic charge/discharge curves (Fig. 5f) depict similar profiles of two platforms at 0.1 A g^{-1}, and Mn_3O_4/PPy-lp gains the best zinc-ion storage capacity. Nevertheless, the gaps in capacity between samples became smaller with the increase of charge/discharge rates (Fig. 5g) owing to the low theoretical specific capacity and superior rate-performance of pure PPy. It is known that an excessive polymer coating slows down the transmission of ions and reduces the capacity of composites, and a moderate PPy coating can well balance the influence of coating on capacity and cycling performance in ZIBs.[45] In our case, the Mn_3O_4/PPy (14.6 wt% PPy) sample delivers a stable capacity of 340.2 mA h g^{-1} when the current density decreases back to 0.1 A g^{-1}, and also the highest capacity of 125.7 mA h g^{-1} after 1000 charge/discharge cycles (Fig. 5h).

3. Conclusion

In summary, a series of ultrafine Mn_3O_4/PPy core–shell nanodot composites (Mn_3O_4/PPy) have been rationally designed and synthesized through an *in situ* polymerization strategy. The PPy content in this core–shell structure was easily tuned by adjusting the pyrrole addition. The optimized Mn_3O_4/PPy nanodot cathode with a PPy ratio of 14.6 wt% displayed superior long-term cycling stability over 1500 cycles with a high capacity retention of 92.5% at 1.0 A g^{-1}. This robust lifespan is almost three times longer than that of pristine Mn_3O_4 nanodots, and also surpasses that of various Mn_3O_4-related cathode materials recently reported. By a systematic study using EIS, *ex situ* XRD, SEM and TEM, we revealed that the enhancement mechanism of the cycling stability is attributed to the increased electron/ion conductivity, alleviated Mn^{2+} dissolution and enhanced structural stability caused by the PPy coating. This organic/manganese oxide composite strategy can also be extended to other energy storage devices, such as pseudocapacitors, solar cells and multivalent ion secondary batteries.

4. Experimental section

Material synthesis

Mn_3O_4 nanodots were prepared according to our previous report.[23] Mn_3O_4/PPy core–shell nanodots were synthesized by using *in situ* polymerization of pyrrole monomers on the surface of Mn_3O_4 nanodots. In a typical synthesis, 0.4 g Mn_3O_4 nanodots were added to 400 mL deionized water with sonication for 15 min to form a well-dispersed solution. 400 μL HCl and 400 μL pyrrole were successively added under stirring, and the reaction was carried out for 24 h at room temperature. The product (marked as Mn_3O_4/PPy) was filtered, washed with water and ethanol several times, and dried in a vacuum for 12 h. Mn_3O_4/PPy nanodots with different amounts of PPy (pyrrole addition was 200 μL and 800 μL) were fabricated with the same method, and are, respectively, denoted as Mn_3O_4/PPy-lp (abbreviation for less pyrrole addition) and Mn_3O_4/PPy-mp (abbreviation for more pyrrole addition).

Materials characterization

The phase structure of samples was determined by powder X-ray diffraction (XRD, Bruker D8 Advance) with the Cu Kα radiation ranging from 10° to 70°. For *ex situ* XRD, the characterization

was carried out before and after charge/discharge cycles at 1.0 A g^{-1}. The morphology and elemental composition of the as-prepared products were obtained by high-resolution transmission electron microscopy (HRTEM, FEI TECNAI G^2 S-TWIN) and field emission scanning electron microscopy (FE-SEM, FEI Nova Nano SEM 450). The chemical bonding conditions were recorded by X-ray photoelectron spectroscopy (XPS, PHI 5000C EACA). The specific surface area was obtained using the Brunauer–Emmett–Teller (BET, Quadrasorb evo) method. The existence of PPy was confirmed by means of thermogravimetric analysis (TGA, TA SDT Q600), Fourier transform infrared spectroscopy (FTIR, Bruker Tensor II), and Raman scattering (Renishaw inVia).

Electrochemical measurement

The electrochemical properties were studied with CR2032 coin cells. In the preparation of the working electrode, 70 wt% active material, 20 wt% acetylene black (AB, conductive additive) and 10 wt% polyvinylidene fluoride (PVDF, binder) were well dispersed in *N*-methyl-2-pyrrolidone (NMP). The slurry was cast on 304L stainless steel (SS, current collector), and then vacuum-dried at 80 °C for 12 h. The mass loading of the active material was about 2 mg cm^{-2}. CR2032 coin cells were assembled with a metallic Zn anode, as-prepared cathode, and Whatman GF/C glass microfiber filter as a separator in an air atmosphere. An aqueous solution containing 2 M $ZnSO_4$/0.2 M $MnSO_4$ was used as the electrolyte. Cyclic voltammetry (CV) curves at varying scan rates of 0.1 to 0.5 mV s^{-1} and electrochemical impedance spectra (EIS) from 100 kHz to 0.01 Hz were obtained on an electrochemical workstation (CHI 660E). Galvanostatic charge–discharge (GCD) tests with a voltage range from 0.8 to 1.9 V, galvanostatic intermittent titration technique (GITT) and cycling tests were performed on a battery test system (LAND CT2001A).

Fabrication of quasi-solid-state batteries

Flexible quasi-solid-state batteries were obtained by sandwiching the separator and electrolyte between the as-prepared cathode and Zn foil anode, and sealing with polyimide (PI) film. Filter paper was used as a separator, and polyvinyl alcohol (PVA) gel containing $Zn(ClO_4)_2$ and $MnSO_4$ served as the electrolyte. Typically, a measure of 3 g PVA was gradually added to 20 mL of 2 M $Zn(ClO_4)_2$ and 0.2 M $MnSO_4$ aqueous solution under magnetic stirring. The solution was treated at 60 °C for 1 h, and then at 90 °C for 2 h in an oil bath. The transparent gel became thick as it cooled down to room temperature. Prior to the assembly, the electrodes and separator were immersed in the gel electrolyte for 5 min, and dried at 40 °C for 30 min.

Conflicts of interest

There are no conflicts to declare.

Acknowledgements

This work was financially supported by the National Natural Science Foundation of China (No. 52171203, 51872051), the Natural Science Foundation of Jiangsu Province (Grant No. BK20211516), the State Key Laboratory of New Ceramic and Fine Processing Tsinghua University (No. KF202102), and the Fundamental Research Funds for the Central Universities (2242021R10119).

Notes and references

1 T. Xiong, Y. Zhang, W. S. V. Lee and J. Xue, *Adv. Energy Mater.*, 2020, **10**, 2001769.
2 Y. Liu, Y. Zhu and Y. Cui, *Nat. Energy*, 2019, **4**, 540–550.
3 T. Kim, W. Song, D. Son, L. K. Ono and Y. Qi, *J. Mater. Chem. A*, 2019, **7**, 2942–2964.
4 P. Canepa, G. S. Gautam, D. C. Hannah, R. Malik, M. Liu, K. G. Gallagher, K. A. Persson and G. Ceder, *Chem. Rev.*, 2017, **117**, 4287–4341.
5 J. Huang, Z. Guo, Y. Ma, D. Bin, Y. Wang and Y. Xia, *Small Methods*, 2019, **3**, 1800272.
6 H. Li, L. Ma, C. Han, Z. Wang, Z. Liu, Z. Tang and C. Zhi, *Nano Energy*, 2019, **62**, 550–587.
7 Y. Tian, Y. An, C. Wei, B. Xi, S. Xiong, J. Feng and Y. Qian, *Adv. Energy Mater.*, 2021, **11**, 2002529.
8 B. Tang, L. Shan, S. Liang and J. Zhou, *Energy Environ. Sci.*, 2019, **12**, 3288–3334.
9 M. Song, H. Tan, D. Chao and H. J. Fan, *Adv. Funct. Mater.*, 2018, **28**, 1802564.
10 G. Fang, J. Zhou, A. Pan and S. Liang, *ACS Energy Lett.*, 2018, **3**, 2480–2501.
11 B. Yong, D. Ma, Y. Wang, H. Mi, C. He and P. Zhang, *Adv. Energy Mater.*, 2020, **10**, 2002354.
12 J. Huang, Z. Wang, M. Hou, X. Dong, Y. Liu, Y. Wang and Y. Xia, *Nat. Commun.*, 2018, **9**, 2906.
13 D. Xu, H. Wang, F. Li, Z. Guan, R. Wang, B. He, Y. Gong and X. Hu, *Adv. Mater. Interfaces*, 2019, **6**, 1801506.
14 J. Wang, K. Cai, S. Shen and J. Yin, *Synth. Met.*, 2014, **195**, 132–136.
15 Y. Chen, W. Ma, K. Cai, X. Yang and C. Huang, *Electrochim. Acta*, 2017, **246**, 615–624.
16 K. Zou, H. Zeng, X. Cao, J. Yuan, G. B. F. C. Alain, S. Xu, H. Li and Y. Long, *Chem.–Asian J.*, 2019, **14**, 4337–4344.
17 B. G. S. Raj, A. M. Asiri, J. J. Wu and S. Anandan, *J. Alloys Compd.*, 2015, **636**, 234–240.
18 Y. Han, T. Wang, T. Li, X. Gao, W. Li, Z. Zhang, Y. Wang and X. Zhang, *Carbon*, 2017, **119**, 111–118.
19 P. Geng, S. Cao, X. Guo, J. Ding, S. Zhang, M. Zheng and H. Pang, *J. Mater. Chem. A*, 2019, **7**, 19465–19470.
20 A. Ramírez, P. Hillebrand, D. Stellmach, M. M. May, P. Bogdanoff and S. Fiechter, *J. Phys. Chem. C*, 2014, **118**, 14073–14081.
21 T. Liu, L. Finn, M. Yu, H. Wang, T. Zhai, X. Lu, Y. Tong and Y. Li, *Nano Lett.*, 2014, **14**, 2522–2527.
22 J. Ji, H. Wan, B. Zhang, C. Wang, Y. Gan, Q. Tan, N. Wang, J. Yao, Z. Zheng, P. Liang, J. Zhang, H. Wang, L. Tao, Y. Wang, D. Chao and H. Wang, *Adv. Energy Mater.*, 2021, **11**, 2003203.
23 L. Jiang, Z. Wu, Y. Wang, W. Tian, Z. Yi, C. Cai, Y. Jiang and L. Hu, *ACS Nano*, 2019, **13**, 10376–10385.

24 Y. Luo, R. Guo, T. Li, F. Li, L. Meng, Z. Yang, Y. Wan and H. Luo, *ChemElectroChem*, 2018, **6**, 690–699.
25 F. Tang, J. Gao, Q. Ruan, X. Wu, X. Wu, T. Zhang, Z. Liu, Y. Xiang, Z. He and X. Wu, *Electrochim. Acta*, 2020, **353**, 136570.
26 F. Tang, T. He, H. Zhang, X. Wu, Y. Li, F. Long, Y. Xiang, L. Zhu, J. Wu and X. Wu, *J. Electroanal. Chem.*, 2020, **873**, 114368.
27 L. Shan, Y. Wang, S. Liang, B. Tang, Y. Yang, Z. Wang, B. Lu and J. Zhou, *InfoMat*, 2021, **3**, 1028–1036.
28 Y. Yang, Y. Tang, G. Fang, L. Shan, J. Guo, W. Zhang, C. Wang, L. Wang, J. Zhou and S. Liang, *Energy Environ. Sci.*, 2018, **11**, 3157–3162.
29 L. Hu, Z. Wu, C. Lu, F. Ye, Q. Liu and Z. Sun, *Energy Environ. Sci.*, 2021, **14**, 4095–4106.
30 Z. Wu, C. Lu, Y. Wang, L. Zhang, L. Jiang, W. Tian, C. Cai, Q. Gu, Z. Sun and L. Hu, *Small*, 2020, **16**, 2000698.
31 Y. Wang, Z. Wu, L. Jiang, W. Tian, C. Zhang, C. Cai and L. Hu, *Nanoscale Adv.*, 2019, **1**, 4365–4372.
32 Z. Liu, Y. Yang, S. Liang, B. Lu and J. Zhou, *Small Struct.*, 2021, 2100119.
33 Z. Wu, Y. Wang, L. Zhang, L. Jiang, W. Tian, C. Cai, J. Price, Q. Gu and L. Hu, *ACS Appl. Energy Mater.*, 2020, **3**, 3919–3927.
34 C. Zhu, G. Fang, J. Zhou, J. Guo, Z. Wang, C. Wang, J. Li, Y. Tang and S. Liang, *J. Mater. Chem. A*, 2018, **6**, 9677–9683.
35 J. Hao, J. Mou, J. Zhang, L. Dong, W. Liu, C. Xu and F. Kang, *Electrochim. Acta*, 2018, **259**, 170–178.
36 Q. Tan, X. Li, B. Zhang, X. Chen, Y. Tian, H. Wan, L. Zhang, L. Miao, C. Wang, Y. Gan, J. Jiang, Y. Wang and H. Wang, *Adv. Energy Mater.*, 2020, **10**, 2001050.
37 T. Takashima, K. Hashimoto and R. Nakamura, *J. Am. Chem. Soc.*, 2012, **134**, 18153–18156.
38 J. Yang, J. Cao, Y. Peng, W. Yang, S. Barg, Z. Liu, I. A. Kinloch, M. A. Bissett and R. A. W. Dryfe, *ChemSusChem*, 2020, **13**, 4103–4110.
39 Y. Zhang, G. Xu, X. Liu, X. Wei, J. Cao and L. Yang, *ChemElectroChem*, 2020, **7**, 2762–2770.
40 Y. Huang, J. Mou, W. Liu, X. Wang, L. Dong, F. Kang and C. Xu, *Nano-Micro Lett.*, 2019, **11**, 49.
41 P. Oberholzer, E. Tervoort, A. Bouzid, A. Pasquarello and D. Kundu, *ACS Appl. Mater. Interfaces*, 2018, **11**, 674–682.
42 B. Lee, H. R. Seo, H. R. Lee, C. S. Yoon, J. H. Kim, K. Y. Chung, B. W. Cho and S. H. Oh, *ChemSusChem*, 2016, **9**, 2948–2956.
43 Z. Li, S. Ganapathy, Y. Xu, Z. Zhou, M. Sarilar and M. Wagemaker, *Adv. Energy Mater.*, 2019, **9**, 1900237.
44 A. Lahiri, L. Yang, G. Li and F. Endres, *ACS Appl. Mater. Interfaces*, 2019, **11**, 45098–45107.
45 H. Qiao, R. Li, Y. Yu, Z. Xia, L. Wang, Q. Wei, K. Chen and Q. Qiao, *Electrochim. Acta*, 2018, **273**, 282–288.
46 W. Wang, D. Wang, G. Wang, M. Zheng and G. Wang, *Adv. Energy Mater.*, 2020, **10**, 1904026.
47 Y. Fang, X. Yu and X. W. D. Lou, *Angew. Chem., Int. Ed.*, 2018, **57**, 9859–9863.
48 H. Chen, W. Zhou, D. Zhu, Z. Liu, Z. Feng, J. Li and Y. Chen, *J. Alloys Compd.*, 2020, **813**, 151812.
49 L. Wang, X. Cao, L. Xu, J. Chen and J. Zheng, *ACS Sustainable Chem. Eng.*, 2018, **6**, 16055–16063.
50 Q. Gao, D. Li, X. Liu, Y. Wang, W. Liu, M. Ren, F. Kong, S. Wang and R. Zhou, *Electrochim. Acta*, 2020, **335**, 135642.
51 M. Sun, D. S. Li, Y. F. Wang, W. L. Liu, M. M. Ren, F. G. Kong, S. J. Wang, Y. Z. Guo and Y. M. Liu, *ChemElectroChem*, 2019, **6**, 2510–2516.
52 Z. Huang, Y. Duan, Q. Jing, M. Sun, B. Tang and S. Shi, *J. Alloys Compd.*, 2021, **864**, 158316.